Interpretation of time reversal focal spots based on point-source homogenization

Zoé Renat, Paul Cupillard, Yann Capdeville

HAL Id: insu-03779249

https://insu.hal.science/insu-03779249

Submitted on 16 Feb 2023

Interpretation of time reversal focal spots based on point-source homogenization

Zoé Renat [1], Paul Cupillard [1] and Yann Capdeville [2]

[1]*RING, GeoRessources/UMR7359, Université de Lorraine/CNRS, 54000 Nancy, France. E-mail:* zoe.renat@univ-lorraine.fr
[2]*LPG, UMR6112, Université de Nantes/CNRS, 44300, Nantes, France*

SUMMARY

The time reversal method is based on the backpropagation of seismic waveforms recorded at a set of receivers. When this set forms a closed surface and the elastic properties of the medium are correct, the seismic energy focuses at the source location, creating a focal spot. Such a spot is smooth in space, whereas the original wavefield usually shows a displacement discontinuity at the source. The goal of this paper is to discuss the link between the focal spot and the original source using the concept of homogenized point source. We show that the backpropagated wavefield is equivalent to the sum of two low-wavenumber fields resulting from the homogenization of the original point source. In other words, the homogenized point source is the equivalent force for producing the focal spot. In addition to the demonstration in the general 3-D heterogeneous case, we present some numerical examples in 2-D.

Key words: Computational seismology; Theoretical seismology; Wave propagation.

1 INTRODUCTION

Seismic event localization and characterization can be performed using multiple methods and various data such as traveltimes or waveforms. Two major families of methods can be distinguished. The first one is based on traveltime picking (e.g. Milne 1886). Because they rely on picking specific seismic phases, traveltime-based methods for determining the location and the mechanism of seismic events (Garmany 1979; Hampson & Russell 1984; Kennett & Sambridge 1992; Sambridge & Mosegaard 2002) are highly sensitive to the quality of the data (i.e. signal-to-noise ratio). Moreover, they disregard significant pieces of information contained in the seismic recordings. To overcome these limitations, waveform-based methods have been developed (e.g. McMechan 1982; Schuster *et al.* 2004; Larmat *et al.* 2006; Grigoli *et al.* 2016; Shi *et al.* 2019; Willacy *et al.* 2019). They rely on complete or partial recorded signals. Their principle is to backpropagate data to either solve a full waveform inverse problem or focus waves at the source location (Li *et al.* 2020). Full waveform inversion for seismic source characterization (e.g. Willacy *et al.* 2019) consists in minimizing a misfit function between observed and synthetic data. To do so, a prior source model is necessary to produce a first synthetic data set. Then the gradient of the misfit function is computed using an adjoint field calculation. The adjoint field is generated by the data residuals at all receivers acting as sources. Other waveform-based approaches include partial waveform stacking (e.g. Kao & Shan 2004), match field processing (e.g. Cros *et al.* 2011), backprojection (e.g. Ishii *et al.* 2007) and time reversal (e.g. Yang & Zhu 2019). They are often called source imaging methods because they all somehow focus waves to create an 'image' of the source. The main advantage of these methods is the absence of prior source model and the direct (i.e. non-iterative) calculation of the solution. However, they may require data processing to clean the input signals, with the notable exception of time reversal, which is poorly sensitive to noise (e.g. Gajewski & Tessmer 2005; Cao *et al.* 2012).

The time reversal technique was introduced by Fink (1992) in ultrasound acoustics. It has been extended to elastic waves by Draeger & Fink (1997). It consists in reversing in time the recorded signals and backpropagating them from the receivers. Under some conditions, the waves follow the inverse path of the forward way and focus at the source position. Such a behaviour can be explained by the invariability of the wavefield through a reverse time operator because of the second-order time derivative of the wave equation

$$\rho \ddot{u}_n - \partial_j(C_{njkl}\partial_k u_l) = f_n \,, \tag{1}$$

with ρ the density, $\boldsymbol{u}$ the displacement, $\ddot{\boldsymbol{u}}$ the second-order time derivative of the displacement, $\boldsymbol{C}$ the elastic tensor and $\boldsymbol{f}$ a force distribution acting in the medium. The result of the backpropagation is a spot at the source location, named the focal spot. The conditions to apply time reversal are the following:

(i) The receivers form a closed surface, called time reversal mirror.

(ii)The time reversal mirror does not perturb the wave propagation.

(iii)The medium is well known. Errors on the velocity model or interface positions would generate modifications in the wave path as compared to the path in the forward process.

(iv)The anelasticity is negligible. Anelastic attenuation would make a first-order time derivative appear in the wave equation so that the time reversibility would not be verified.

In practice, conditions (i), (iii) and (iv) are difficult to satisfy: there is no continuous surfaces of receivers in the underground, the velocity model presents uncertainties and the earth is anelastic. Nevertheless, some solutions exist to overcome these difficulties. For instance, Cassereau & Fink (1992) developed a mathematical model for time reversal with a plane mirror in ultrasound acoustics. In geophysics, Li & van der Baan (2016) showed that microseismic events can be localized using a single well as time reversal mirror. To improve this kind of results, Bazargani & Snieder (2016) presented an optimization of time reversal which mitigates the incompleteness of the mirror. More recently, Finger & Saenger (2021) used surface data as a plane mirror to locate microseisms in a geothermal reservoir. As for the influence of the velocity model uncertainties on the focalization, Gajewski & Tessmer (2005) carried out a sensitivity study a in 2-D subsurface model. Using two sets of synthetics data (one from the true medium and the other from a random medium which contains the same range of velocity), they showed that the focal spot obtained with the second set of data is found 20 m above the true source location and 8 ms after the centroid time. They also performed a test with a smooth velocity medium similar to those obtained from tomography. In this medium, the focal spot is only shifted in time. Furthermore, Bazargani & Snieder (2016) tested the impact of the velocity uncertainties on both their optimized time reversal and the classical time reversal approach. Between the two, classical time reversal is less sensitive to velocity uncertainty. As for the anelasticity, Zhu (2014) and Bai *et al.* (2019) proposed a mathematical solution to compensate attenuation and validated it using numerical experiments of time reversal for source localization.

Time reversal is used in multiple domains such as medicine (e.g. Fink 2015), underwater communication (e.g. Kuperman *et al.* 1998) and geosciences (e.g. Li & van der Baan 2016). In the latter domain, applications mainly deal with earthquake localization and characterization: Larmat *et al.* (2008) applied it on glacial earthquakes, Douma *et al.* (2015), Li & van der Baan (2016), Yang & Zhu (2019), Finger & Saenger (2021) on microseismicity and Rietbrock & Scherbaum (1994) to characterize an aftershock series. Time reversal can also be used to follow fluid displacements in the underground using tremors (Steiner *et al.* 2008). Other studies investigate time reversal for detecting scatterers (Givoli & Turkel 2012; Shustak & Landa 2017; Rabinovich *et al.* 2018) or for reconstructing the complete wavefield (van Manen *et al.* 2006; Masson *et al.* 2014; Masson & Romanowicz 2017). In addition to the location, the focal spot obtained with time reversal possibly contains pieces of information on the source mechanism and the medium heterogeneities at the source. However, the question of the link between this focal spot and the details of the source of the earthquake still remains. Some pieces of answers exist in the literature: Kremers *et al.* (2011) succeeded to extract the centroid time in addition to the spatial location in the case of a single point source, but not in the case of multiple sources; Chambers *et al.* (2014) proposed a method to recover the space and time location as well as the moment tensor of a source; Nakahara & Haney (2015) established a theoretical link between the focal spot and the point spread function. Our work is aligned with all these previous work on the focal interpretation and others.

In this paper, we present a new way to interpret the time reversal focal spot in the light of point-source homogenization. Our interpretation is a complement to previous theoretical contributions (e.g. Kawakatsu & Montagner 2008; Kiser *et al.* 2011; Fukahata *et al.* 2014; Douma & Snieder 2014; Anderson *et al.* 2015; Nakahara & Haney 2015) in the long-term effort for relating source images to source mechanisms. Essentially, we show how the proper upscaling of the point-source model can lead to time reversal focal spots, which is a first step toward the ambition of downscaling time reversal results in terms of source mechanism. First, we present the theory of time reversal and a simple synthetic example of the problem we want to tackle. Second, we interpret the time reversal wavefield using the theory of point-source homogenization. Then our result is illustrated with numerical 2-D examples involving (i) an explosion, (ii) *P* and *S* waves, (iii) an extended source and (iv) a heterogeneous case. Finally, we discuss the implications of our results and the current limitations for applying it in real cases.

2 TIME REVERSAL

2.1 Theory

Relying on the four conditions presented in the Introduction, we can go deeper into the physics of time reversal. Let us first invoke the representation theorem (Masson *et al.* 2014), which reads in the frequency domain as

$$u_i(x) = \int_V G_{in}(x, x') f_n(x') \, dV$$

$$+ \oint_S G_{in}(x, x') \, n_j \, C_{njkl} \, \partial'_k u_l(x') \, dS'$$

$$- \oint_S u_n(x') \, n_j \, C_{njkl} \, \partial'_k G_{il}(x, x') \, dS', \tag{2}$$

with $G(x, x')$ the Green tensor between the points x and x', n the unit normal vector to the closed surface S and V the volume bounded by S (Fig. 1). This theorem establishes that the displacement at any position x can be retrieved from three terms:

Figure 1. Setup of the representation theorem. The star represents a point source. n is a unit-vector normal to the closed surface S. The theorem allows us calculating the displacement at any point in the volume V.

(i) a volume integral which involves the body force $\boldsymbol{f}$;

(ii) a surface integral which involves the normal traction $T_n = n_j C_{njkl} \partial_k u_l$ at the surface S;

(iii) a surface integral which involves the tensor $M_{kl} = u_n n_j C_{njkl}$ at the surface S.

In the frequency domain, reversing the time means taking the complex conjugate, denoted by *. Applying this to eq. (2) and benefitting from the Green tensor reciprocity, the time reversed displacement is given by

$$
\begin{aligned}
u_i^*(\boldsymbol{x}) = & \int_V G_{in}(\boldsymbol{x}, \boldsymbol{x}') f_n^*(\boldsymbol{x}') dV \\
& + \oint_S G_{in}(\boldsymbol{x}, \boldsymbol{x}') n_j C_{njkl} \partial_k' u_l^*(\boldsymbol{x}') dS' \\
& - \oint_S u_n^*(\boldsymbol{x}') n_j C_{njkl} \partial_k' G_{il}(\boldsymbol{x}, \boldsymbol{x}') dS'.
\end{aligned}
\tag{3}
$$

When implementing this numerically, the surface S is discretized and the integrals are approximated by a quadrature:

$$
\begin{aligned}
u_i^*(\boldsymbol{x}) = & \int_V G_{in}(\boldsymbol{x}, \boldsymbol{x}') f_n^*(\boldsymbol{x}') dV \\
& + \sum_{r=1}^{n} \alpha_r G_{in}(\boldsymbol{x}, \boldsymbol{x}_r') T_n^*(\boldsymbol{x}'_r) \\
& - \sum_{r=1}^{n} \alpha_r M_{kl}^*(\boldsymbol{x}'_r) \partial_k' G_{il}(\boldsymbol{x}, \boldsymbol{x}_r'),
\end{aligned}
\tag{4}
$$

with $\boldsymbol{x}'_r$ ($r = 1,...,n$) the quadrature nodes with the associated weight α_r. Applying the Dirac property $f(\boldsymbol{x}) = \int_V f(\boldsymbol{x}') \delta(\boldsymbol{x}' - \boldsymbol{x}) d\boldsymbol{x}'$ to the last two terms and integrating by part the last term, we obtain

$$
\begin{aligned}
u_i^*(\boldsymbol{x}) = & \int_V G_{in}(\boldsymbol{x}, \boldsymbol{x}') f_n^*(\boldsymbol{x}') dV \\
& + \sum_{r=1}^{n} \int_V \alpha_r G_{in}(\boldsymbol{x}, \boldsymbol{x}') T_n^*(\boldsymbol{x}') \delta(\boldsymbol{x}' - \boldsymbol{x}'_r) dV' \\
& + \sum_{r=1}^{n} \int_V \alpha_r G_{il}(\boldsymbol{x}, \boldsymbol{x}') \partial_k' [M_{kl}^*(\boldsymbol{x}') \delta(\boldsymbol{x}' - \boldsymbol{x}'_r)] dV'.
\end{aligned}
\tag{5}
$$

This last equation means that we can reconstruct the time reversed displacement $\boldsymbol{u}^*$ from

(i) the time reversed body force $\boldsymbol{f}^*$, which actually acts as a sink;

(ii) n monopoles derived from the time reversed traction $\boldsymbol{T}^*$ at each point $\boldsymbol{x}_r$ on the surface S:

$$
\boldsymbol{f}_r^m(\boldsymbol{x}) = \boldsymbol{T}^*(\boldsymbol{x}) \delta(\boldsymbol{x} - \boldsymbol{x}_r) \alpha_r ;
\tag{6}
$$

(iii) n dipoles derived from the time reversed moment tensor $\boldsymbol{M}^*$ at each point $\boldsymbol{x}_r$ of the surface S:

$$
\boldsymbol{f}_r^d(\boldsymbol{x}) = \nabla \cdot \left[\boldsymbol{M}^*(\boldsymbol{x}) \delta(\boldsymbol{x} - \boldsymbol{x}_r) \right] \alpha_r .
\tag{7}
$$

In the time domain, eq. (5) can be summarized as follows:

$$
\boldsymbol{u}(\boldsymbol{x}, T - t) = \boldsymbol{u}^{tr}(\boldsymbol{x}, t) + \boldsymbol{u}^s(\boldsymbol{x}, t)
\tag{8}
$$

with $\boldsymbol{u}(\boldsymbol{x}, T - t)$ the forward displacement reversed in time (T being the propagation duration), $\boldsymbol{u}^{tr} = \boldsymbol{u}^m + \boldsymbol{u}^d$ the displacement generated from the closed surface ($\boldsymbol{u}^m$ being the displacement created by the monopoles and $\boldsymbol{u}^d$ the displacement created by the dipoles) and $\boldsymbol{u}^s$ the displacement generated by the sink force. $\boldsymbol{u}^{tr}$ is the field that can be computed in practice because the force $\boldsymbol{f}$ is not available (this is our unknown). As a consequence, we do not reconstruct $\boldsymbol{u}$, but a smooth version of it, as we will see in the following.
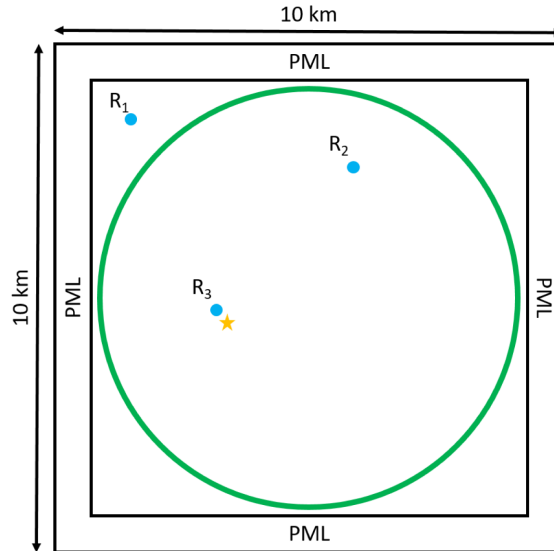
Figure 2. Set up of our first numerical experiment. The medium is homogeneous with $V_p = 3200 \, \text{m s}^{-1}$, $V_s = 2000 \, \text{m s}^{-1}$ and $\rho = 2200 \, \text{kg m}^{-3}$. The source (orange star) is positioned in the area defined by the green circle which represents the closed surface on which the signal is recorded. The medium is surrounded by absorbing boundaries. The blue discs mark three positions at which the wavefield is output in each simulation (backward and forward) to do waveform comparisons.

2.2 A simple example in 2-D

To shed a first light on the similarities and discrepancies between $\boldsymbol{u}$ and $\boldsymbol{u}^{tr}$, we compute the two fields in a simple homogeneous 2-D case with a perfect time reversal mirror. The model is a $10 \, \text{km} \times 10 \, \text{km}$ square with absorbing boundaries (PML). The source is a point source equipped with the identity moment tensor (i.e. an explosion) and a Ricker wavelet time function. The source and closed surface positions are summarized in Fig. 2. The simulations are performed using the spectral element software SPECFEM2D (Komatitsch & Vilotte 1998; Komatitsch & Tromp 1999) following a three steps procedure:

(i) creation of the closed surface of receivers and estimation of the integration weights α_r and the normal vectors $\boldsymbol{n}_r$;
(ii) forward simulation using SPECFEM2D and storage of both the displacement and the stress tensor at each receiver position to use them as input for the next step;
(iii) backward simulation using SPECFEM2D, to obtain the focal spot.

Fig. 3 shows the forward simulation $\boldsymbol{u}$ and the backward simulation $\boldsymbol{u}^{tr}$ obtained with both monopole and dipole terms applied together. In the backward simulation, no waves are generated beyond the closed surface S (Fig. 3 at t_4). On the contrary, in the volume V embedded by the closed surface S, we observe a wavefield which converges to the source location and forms a focal spot. At t_4, t_3, t_2, this wavefield perfectly corresponds to the forward displacement $\boldsymbol{u}$. After (in reverse time) t_2, the backward wavefield diverges and no longer corresponds to the forward wavefield. If the sink term was implemented, the energy would be absorbed at the source location and the wavefield would match the forward simulation at all times (Masson *et al.* 2014). The absence of the sink actually creates the focal spot which is different from the forward near-field. To go further, we compare the displacement at three specific positions: beyond the closed surface, in the volume V far from the source position and in the volume V near the source position (Fig. 2).

When the receiver lays beyond the recording surface (Fig. 4, top row), the backward displacement is zero, meaning that $\boldsymbol{u}^m = -\boldsymbol{u}^d$. When the receiver is in the volume V and more than one wavelength away to the source location (Fig. 4, middle row), the backward displacement perfectly matches the forward displacement. Finally, when the receiver is less than one wavelength away to the source location (Fig. 4, bottom row), the backward displacement does not match the forward displacement: there is a smooth focal spot instead of a displacement discontinuity at the focalization time (i.e. the centroid time) in the backward simulation. To better see what happens near the source, we record the displacement along a receiver line positioned at the source depth and plot the displacement along this line for different time steps (Fig. 5). The displacement at t_4 and t_3 confirms the results presented in the previous figures: the backward displacement matches the forward displacement, even at the source location. However, at earlier times (t_1 and t_2), the two displacements do not match. The backward displacement is smoother than the forward displacement which presents a sharp discontinuity at the source position. This discontinuity corresponds to the seismic rupture process, which is mathematically modelled by a space derivative of a Dirac function. In theory, this discontinuity is even sharper than what we observed in Fig. 5 because the simulation is limited by the mesh resolution (Capdeville 2021).

In smooth media such as the homogeneous one we are considering in this subsection, the smoothness of the focal spot is easily explained by the fact that $\boldsymbol{u}^{tr}$ is generated by two smooth forces (eqs 6 and 7) so $\boldsymbol{u}^m$ and $\boldsymbol{u}^d$ are smooth. In more complex media which contains small-scale features and scatterers, the smoothness of the focal spot can be explained by the diffraction limit $\lambda_{min}/2$ (Cassereau & Fink 1992). Nevertheless, when specific scatterers (e.g. split ring resonators) lie near the source, this limit can be beaten and super-resolution (i.e.
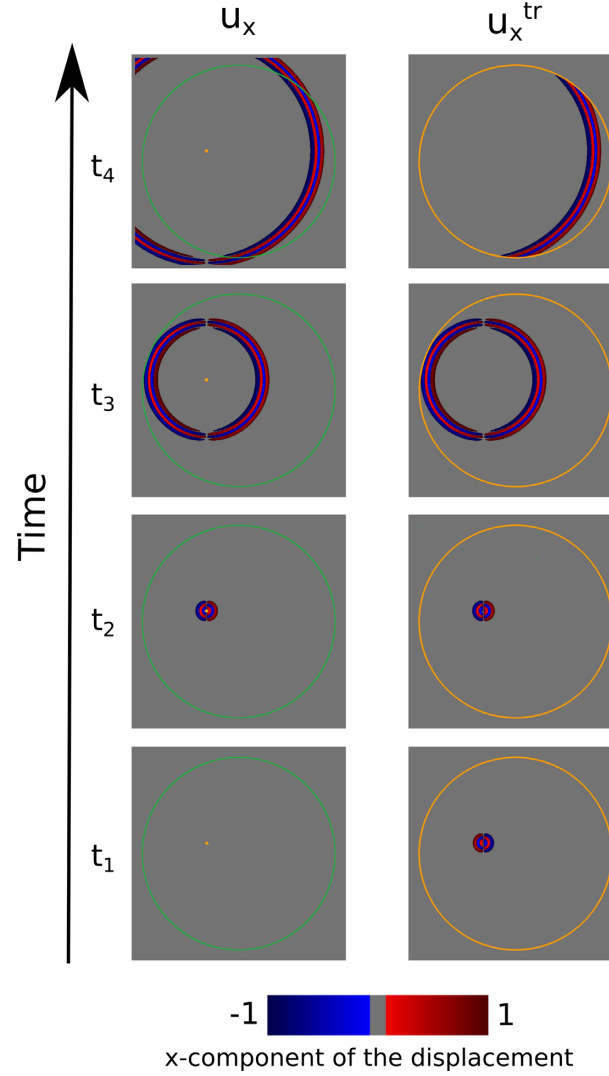
Figure 3. Snapshots of the *x*-component of the normalized displacement. The left-hand side column represents the forward displacement ***u***. The right-hand side column is the backward displacement ***u**^{tr}* generated by monopoles (eq. 6) and dipoles (eq. 7). The receivers are represented in green, and the sources in orange.

subwavelength focusing) can be obtained (de Rosny & Fink 2002; Borcea *et al.* 2003; Fink 2006; Lerosey *et al.* 2007; Gelius & Asgedom 2011; Schuster *et al.* 2012; Zhao *et al.* 2016). In the present work, we disregard this case and put this interesting property of the time reversal on the side.

From eq. (8), we can write the time reversal displacement as

$$\boldsymbol{u}^{tr}(\boldsymbol{x}, t) = \boldsymbol{u}(\boldsymbol{x}, T - t) - \boldsymbol{u}^{s}(\boldsymbol{x}, t), \tag{9}$$

which means that the smooth time reversal wavefield can also be seen as a combination of two discontinuous wavefields: the forward and the sink. It is not trivial to prove that such a combination can generate a continuous wavefield. In the following part, we show that it can be demonstrated thanks to the theory of point-source homogenization developed by Capdeville (2021).

3 POINT-SOURCE HOMOGENIZATION

3.1 Principle and mathematics

The non-periodic homogenization has proved to enable the computation of accurate effective properties for the elastic wave equation, which allows to perform wave simulations in complex geological models using coarse meshes and a tractable computational cost (e.g. Capdeville *et al.* 2010; Cupillard & Capdeville 2018; Capdeville *et al.* 2020). Homogenization consists in low-pass filtering relevant quantities derived from the model to be smoothed, namely the strain and the stress *concentrators*. To define the low-pass filter F^{ϵ_0}, a scaling parameter ϵ_0 is
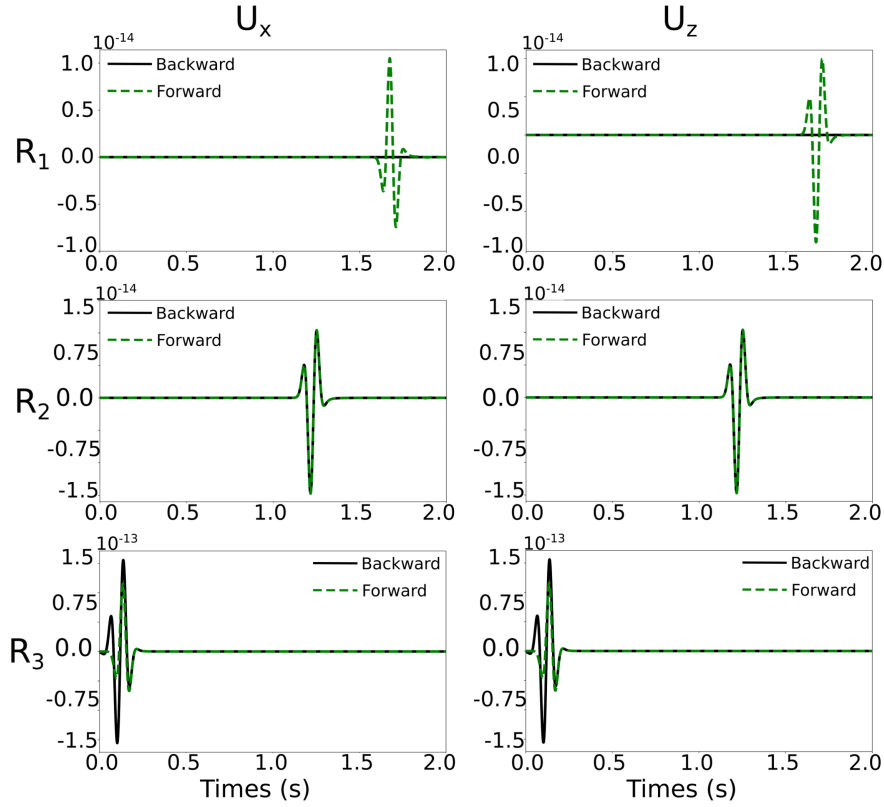
Figure 4. Comparison of forward u and backward u^{tr} waveforms at three different receiver positions (Fig. 2). The black line represents the backward displacement and the green dashed line the forward displacement. The first column shows the *x*-component and the second column shows the *z*-component.

introduced:

$$\epsilon_0 = \frac{\lambda_0}{\lambda_{\min}}, \tag{10}$$

where λ_0 is the wavelength under which the scales are considered as small (defined by the user) and $\lambda_{\min}$ the minimum wavelength to be propagated in the model.

Capdeville (2021) recently applied homogenization to a point source. The idea is to filter the high-wavenumber content of a point source in order to compute a smooth effective source. Point source is a classic model for representing the mechanism of an earthquake. There are two major types of point sources: the single force f (eq. 11) and the couple force or stress source τ (eq. 12, Aki & Richards 2002):

$$f(x, t) = F\delta(x - x_0)g(t), \tag{11}$$

$$\tau(x, t) = M\delta(x - x_0)g(t), \tag{12}$$

with F a force vector, M a moment tensor, g a source time function and δ the Dirac function. The homogenization aims at separating the small scales (hereafter denoted by the y variable) and the large scales (hereafter denoted by the x variable) within both the displacement and the stress fields. In other words, the homogenization looks for the solution of the elastodynamic problem in the following form: $u(x, y, t)$ and $\sigma(x, y, t)$. To do so, the method relies on asymptotic expansion of the two fields:

$$u(x, t) = u_0(x, y, t) + \epsilon_0 u_1(x, y, t) + \epsilon_0^2 u_2(x, y, t) + \cdots, \tag{13}$$

$$\sigma(x, t) = \sigma_0(x, y, t) + \epsilon_0 \sigma_1(x, y, t) + \epsilon_0^2 \sigma_2(x, y, t) + \cdots, \tag{14}$$

where the two space variables relate through the scaling parameter ϵ_0: $y = \frac{x}{\epsilon_0}$. In what follows, we focus on the couple force, the derivation for the single force case being similar (Capdeville 2021).

First of all, it can be shown (Appendix A) that a Dirac function can be decomposed as

$$\delta(x) = \frac{1}{\epsilon_0}(I - F)(\delta)(y) + F^{\epsilon_0}(\delta)(x), \tag{15}$$
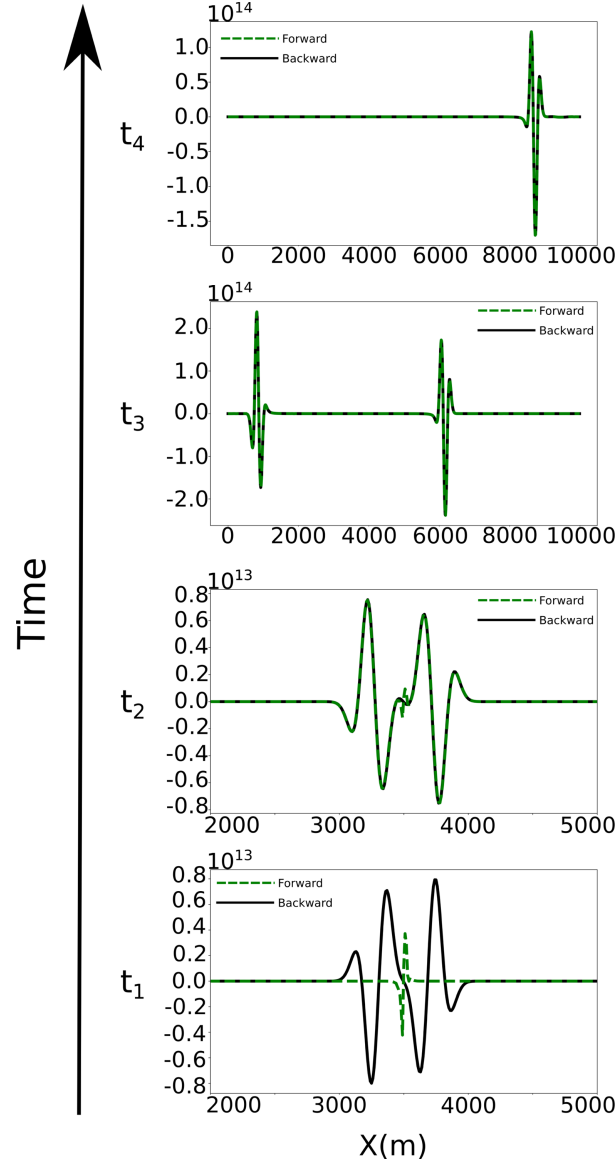
Figure 5. Plot of the *x*-component of the displacement along a line of receivers at the source depth for four different time steps. The steps are those chosen on Fig. 2. The black line represents the backward displacement $\boldsymbol{u}$ and the dashed green line the forward displacement $\boldsymbol{u}^{tr}$.

where F^{ϵ_0} is the low-pass filter for the $\boldsymbol{x}$ variable (muting the wavenumbers larger than $\frac{1}{\lambda_0}$) and F the low-pass filter for the $\boldsymbol{y}$ variable (muting the wavenumbers larger than $\frac{1}{\lambda_{\min}}$). As a consequence, we can assume that the couple force can be expanded as

$$\tau(\boldsymbol{x}, t) = \frac{1}{\epsilon_0} \tau_{-1}(\boldsymbol{x}, \boldsymbol{y}) g(t) + \tau_0(\boldsymbol{x}) g(t). \tag{16}$$

To obtain the coefficients τ_{-1} and τ_0, we introduce the expansions (13), (14) and (16) into the wave equation and Hooke's law, which leads to

$$\rho \ddot{\boldsymbol{u}}_i - \nabla_x \cdot \boldsymbol{\sigma}_i - \nabla_y \cdot \boldsymbol{\sigma}_{i+1} = \boldsymbol{0}, \tag{17}$$

$$\boldsymbol{\sigma}_i = \boldsymbol{c} : \left(\nabla_x(\boldsymbol{u}_i) + \nabla_y(\boldsymbol{u}_{i+1}) \right) - \tau_i, \tag{18}$$

with $\boldsymbol{c}$ the elastic tensor and i denoting each order in the expansions. For sake of simplicity, we here assume that $\boldsymbol{c}$ is smooth, that is, $\boldsymbol{c} = \boldsymbol{c}(\boldsymbol{x})$ (see Capdeville 2021, sections 2.4 and 3.4, for a discussion on how handling small-scale mechanical properties in source homogenization). Solving the system (17) and (18) for each i, we end up with

$$\boldsymbol{u}(\boldsymbol{x}, \boldsymbol{y}, t) = \boldsymbol{u}_0(\boldsymbol{x}, t) + \boldsymbol{\theta}(\boldsymbol{y}) g(t) + \mathcal{O}(\epsilon_0). \tag{19}$$

$\boldsymbol{\theta}(\boldsymbol{y})$ is called the corrector; it contains only small scales. Eq. (19) shows that the wavefield can be decomposed into a smooth wavefield $\boldsymbol{u}_0$ which propagates in the medium- and a high-wavenumber part $\boldsymbol{\theta}$ which is not constrained by the dispersion relation. The corrector indeed
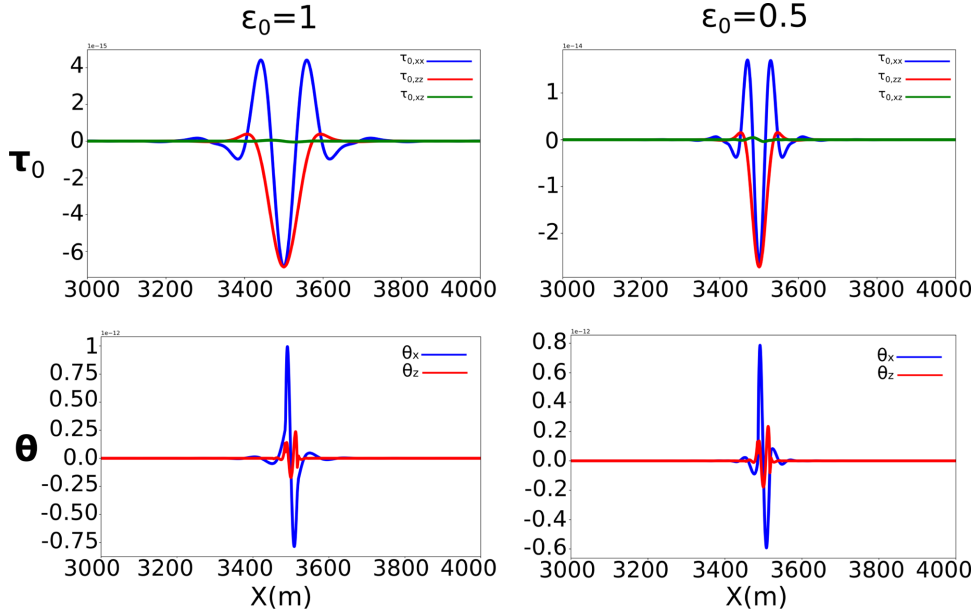
Figure 6. Results of point-source homogenization for $M = I$ in a 2-D homogeneous medium using two values of ϵ_0. The top row represents the effective couple force $\boldsymbol{\tau_0}$ and the bottom row shows the corrector $\boldsymbol{\theta}$ along the x-axis.

satisfies the static partial differential equation

$$\nabla_y \cdot \boldsymbol{c} : \nabla_y(\boldsymbol{\theta}) = \nabla_y \cdot \boldsymbol{\tau}_{-1}. \tag{20}$$

with periodic boundary conditions. As for the zeroth-order displacement $\boldsymbol{u}^0(\boldsymbol{x}, t)$, it is the solution of the effective elastodynamic problem

$$\rho \ddot{\boldsymbol{u}}_0 - \nabla_x \cdot \boldsymbol{\sigma}_0 = \boldsymbol{0}, \tag{21}$$

$$\boldsymbol{\sigma}_0 = \boldsymbol{c} : \nabla_x(\boldsymbol{u_0}) - \boldsymbol{\tau_0}\, g(t). \tag{22}$$

The procedure to determine the coefficients $\boldsymbol{\tau}_0$ and $\boldsymbol{\tau}_{-1}$ in practice is to solve eq. (20) assuming a starting stress $\boldsymbol{\tau}_{-1,s} = \boldsymbol{M}\delta(\boldsymbol{y})$ and that all the variations of $\boldsymbol{c}$ are small so that $\boldsymbol{c} = \boldsymbol{c}(\boldsymbol{y})$ (whatever the true distribution of scales in $\boldsymbol{c}$ is). Doing so, we obtain the starting corrector $\boldsymbol{\theta}_s(\boldsymbol{y})$. By filtering it, the large and small scales can be separated within two quantities: the corrector $\boldsymbol{\theta}$ for the small scales and the source potential $\boldsymbol{\psi}$ for the large scales:

$$\boldsymbol{\theta}(\boldsymbol{y}) = (I - F)\boldsymbol{\theta}_s(\boldsymbol{y}), \tag{23}$$

$$\boldsymbol{\psi}(\boldsymbol{x}) = F^{\epsilon_0}\left[\boldsymbol{\theta}_s\left(\frac{\boldsymbol{x}}{\epsilon_0}\right)\right]. \tag{24}$$

From the potential and the corrector, $\boldsymbol{\tau}_0$ and $\boldsymbol{\tau}_{-1}$ are built:

$$\boldsymbol{\tau}_{-1}(\boldsymbol{x}, \boldsymbol{y}) = \boldsymbol{c}(\boldsymbol{x}) : \nabla_y(\boldsymbol{\theta}(\boldsymbol{y})), \tag{25}$$

$$\boldsymbol{\tau}_0(\boldsymbol{x}) = \boldsymbol{c}(\boldsymbol{x}) : \nabla_x(\boldsymbol{\psi}(\boldsymbol{x})). \tag{26}$$

From $\boldsymbol{\tau_0}$, we easily derive the effective force $\boldsymbol{f}_0$ to apply in the effective wave propagation problem (21) and (22) to get $\boldsymbol{u}_0$. Introducing (26) into (22) and then (22) into (21), we indeed have

$$\rho \ddot{\boldsymbol{u}}_0 - \nabla \cdot \boldsymbol{c} : \nabla(\boldsymbol{u}_0) = \boldsymbol{f}_0 \tag{27}$$

with $\boldsymbol{f}_0(\boldsymbol{x}, t) = -\nabla \cdot \boldsymbol{\tau}_0(\boldsymbol{x})g(t)$.

Fig. 6 shows $\boldsymbol{\tau}_0$ and $\boldsymbol{\theta}$ for $M = I$ in a 2-D homogeneous case. We test two values for ϵ_0: $\epsilon_0 = 1$ to see what happens when filtering at the minimum wavelength and $\epsilon_0 = 0.5$ because it corresponds to the diffraction limit. The top row shows that the spatial spread of the effective couple force decreases with ϵ_0. Furthermore, we see that the potential $\boldsymbol{\psi}$ holds the large scales whereas the corrector $\boldsymbol{\theta}$ contains the small scales. Fig. 7 shows that the corrector contributes to the displacement only near the source. When this latter is emitting (Fig. 7, top row), the corrector has a major role because it contains the discontinuity at the source. When the source stops emitting (Fig. 7, bottom row), there is no difference between the reference and the zeroth-order displacement. In the next section, we link this theory to the focal spot of the time reversal.
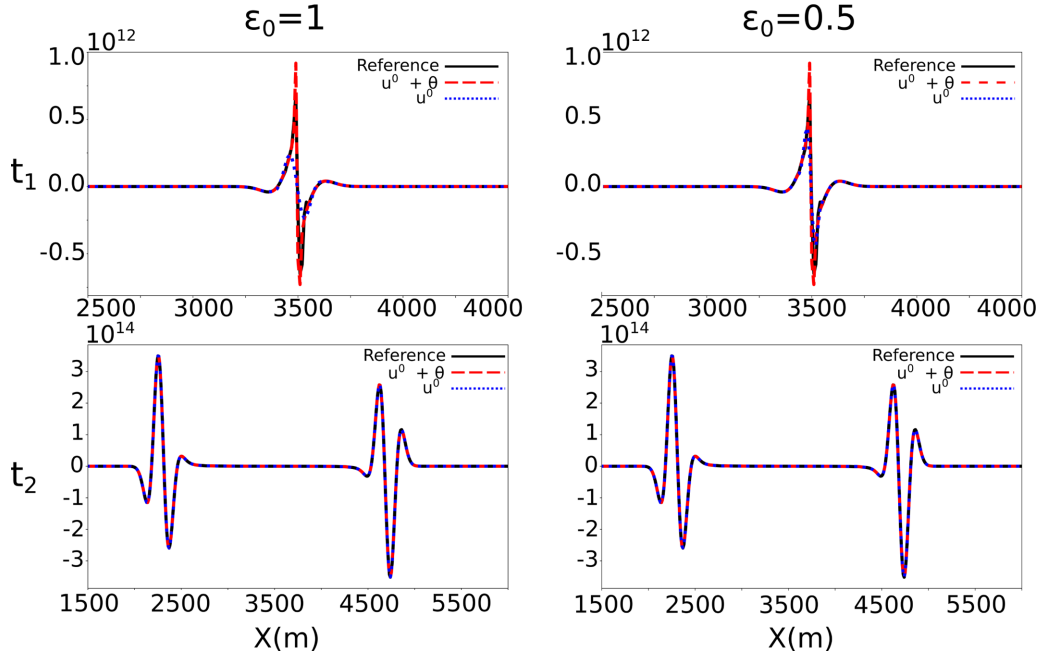
Figure 7. Comparison of the displacement generated by the homogenized point source with a reference displacement computed in a fine mesh at the source. Two values of ϵ_0 are shown. The curves represent the *x*-component of the displacement at two different time steps: t_1 is a time near the source burst and t_2 is a time when the source has stopped emitting.

3.2 Application to time reversal

In the case of a stress source (12), the forward displacement $\boldsymbol{u}$ is the response to the body force

$$\boldsymbol{f}(\boldsymbol{x}, t) = -\nabla \cdot \boldsymbol{\tau}(\boldsymbol{x}, t) = -\boldsymbol{M} \cdot \nabla \delta(\boldsymbol{x} - \boldsymbol{x_0}) g(t). \tag{28}$$

As we just saw, this displacement can be decomposed following eq. (19). By reversing it in time, we can write the first term of the right-hand side of eq. (9) as

$$\boldsymbol{u}(\boldsymbol{x}, \boldsymbol{y}, T - t) = \boldsymbol{u}_0(\boldsymbol{x}, T - t) + \boldsymbol{\theta}(\boldsymbol{y}) g(T - t) + \mathcal{O}(\epsilon_0). \tag{29}$$

For the sink displacement $\boldsymbol{u}^s(\boldsymbol{x}, t)$, the body force is

$$\boldsymbol{f}^s(\boldsymbol{x}, t) = -\boldsymbol{M} \cdot \nabla \delta(\boldsymbol{x} - \boldsymbol{x_0}) g(T - t). \tag{30}$$

Using decomposition (19) again, we can then write the second term of the right-hand side of eq. (9) as

$$\boldsymbol{u}^s(\boldsymbol{x}, \boldsymbol{y}, t) = \boldsymbol{u}_0^s(\boldsymbol{x}, t) + \boldsymbol{\theta}^s(\boldsymbol{y}) g(T - t) + \mathcal{O}^s(\epsilon_0). \tag{31}$$

Introducing (29) and (31) into eq. (9), the time reversal displacement can be expressed as

$$\boldsymbol{u}^{tr}(\boldsymbol{x}, t) = \boldsymbol{u}_0(\boldsymbol{x}, \boldsymbol{T} - \boldsymbol{t}) + \boldsymbol{\theta}(\boldsymbol{y}) g(T - t) + \mathcal{O}(\epsilon_0) - \boldsymbol{u}_0^s(\boldsymbol{x}, t) - \boldsymbol{\theta}^s(\boldsymbol{y}) g(T - t) - \mathcal{O}^s(\epsilon_0). \tag{32}$$

The forces which generate the forward and the sink displacement (i.e. eqs 28 and 30) have the exact same spatial part, so the two correctors $\boldsymbol{\theta}$ and $\boldsymbol{\theta}^s$ are equal. Therefore, eq. (32) reduces to

$$\boldsymbol{u}^{tr}(\boldsymbol{x}, t) = \boldsymbol{u}_0(\boldsymbol{x}, T - t) - \boldsymbol{u}_0^s(\boldsymbol{x}, t) + \mathcal{O}'(\epsilon_0). \tag{33}$$

This last equation is the main result of this paper. It demonstrates the smoothness of the time reversal wavefield, including the focal spot, in a new way. Eq. (33) indeed shows that the backpropagated wavefield can be seen as the sum of two low-wavenumber fields resulting from the homogenization of the original point source. In other words, the homogenized point source is the equivalent force for producing the time reversal wavefield, including the focal spot. To better understand how eq. (33) works, we compute $\boldsymbol{u}_0$ and $\boldsymbol{u}_0^s$ in the simple 2-D case presented in Section 2.2. The point source is homogenized using $\epsilon_0 = 0.5$ and all the wave simulations are performed in the same mesh. Fig. 8 (left-hand column) shows three snapshots of $\boldsymbol{u}_0$, $\boldsymbol{u}_0^s$, $\boldsymbol{u}_0 - \boldsymbol{u}_0^s$ and $\boldsymbol{u}^{tr}$ along a horizontal line. At $t < T - 2\tau_b$ (top row), the sink did not start acting yet, so $\boldsymbol{u}_0^s(\boldsymbol{x}, t) = \boldsymbol{0}$ and the time reversal displacement $\boldsymbol{u}^{tr}(\boldsymbol{x}, t)$ is equal to the zeroth-order forward displacement $\boldsymbol{u}_0(\boldsymbol{x}, T - t)$. At $t > T$ (bottom row), $\boldsymbol{u}_0(\boldsymbol{x}, T - t)$ vanishes and the time reversal displacement $\boldsymbol{u}^{tr}(\boldsymbol{x}, t)$ is the opposite of the zeroth-order sink displacement $-\boldsymbol{u}_0^s(\boldsymbol{x}, t)$. The middle row shows that in the time interval $T - 2\tau_b < t < T$, which corresponds to the focalization, the time reversal displacement is a combination of the two non-zero displacements $\boldsymbol{u}_0$ and $\boldsymbol{u}_0^s$. This numerical experiment illustrates eq. (33). Moreover, it allows us defining the focal spot as an extended object both in space and time: the focal spot begins when the displacement is different from the forward displacement and ends when the displacement is the opposite of the sink displacement.
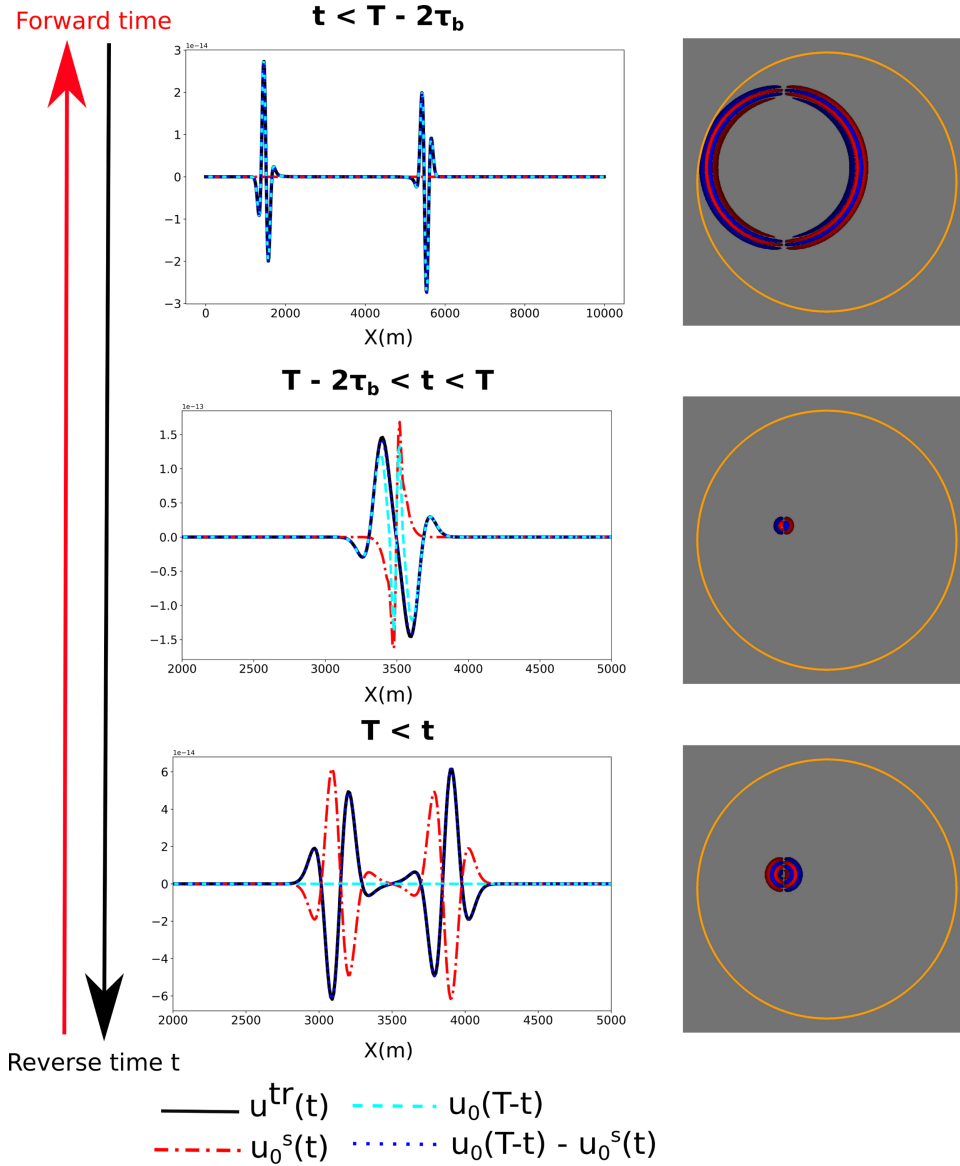
Figure 8. Comparison of the time reversal displacement $\boldsymbol{u}^{tr}$ to the difference between the two zeroth-order displacements $\boldsymbol{u}_0$ and $\boldsymbol{u}_0^s$. The curves (left) and the time reversal wavefield (right) represent the x-component at three different reverse time t. T is the forward simulation duration and τ_b is the centroid time of the source.

4 NUMERICAL ILLUSTRATIONS

To further illustrate the mathematical result of the previous part, we apply it to more complex synthetic cases. In the first one, we add an S wave by taking $\boldsymbol{M} \neq \boldsymbol{I}$; in the second one, we model an extended source using multiple point sources; in the third, we consider a heterogeneous medium.

4.1 *P* and *S* waves in a homogeneous medium

Here we add an S wave to the numerical experiment described in the previous parts. To do so, we input the following randomly chosen moment tensor:

$$\boldsymbol{M} = \begin{bmatrix} -2 & 1 \\ 1 & 1 \end{bmatrix}. \tag{34}$$

The source time function $g(t)$ is a Ricker wavelet with a dominant frequency of $10\,\mathrm{Hz}$, leading to a minimum wavelength of $66\,\mathrm{m}$.

Fig. 9 compares the backward simulation $\boldsymbol{u}^{tr}$ to the forward simulation $\boldsymbol{u}$ (see the two wavefields on the left-hand side and the curves in the central column). As expected, the introduction of an S wave does not alter the conclusions we drew in Section 2.2. The time reversal still succeeds in reconstructing the far field (e.g. at t_3 and t_4). On the contrary, in the focalization time interval (e.g. at t_2), the backward
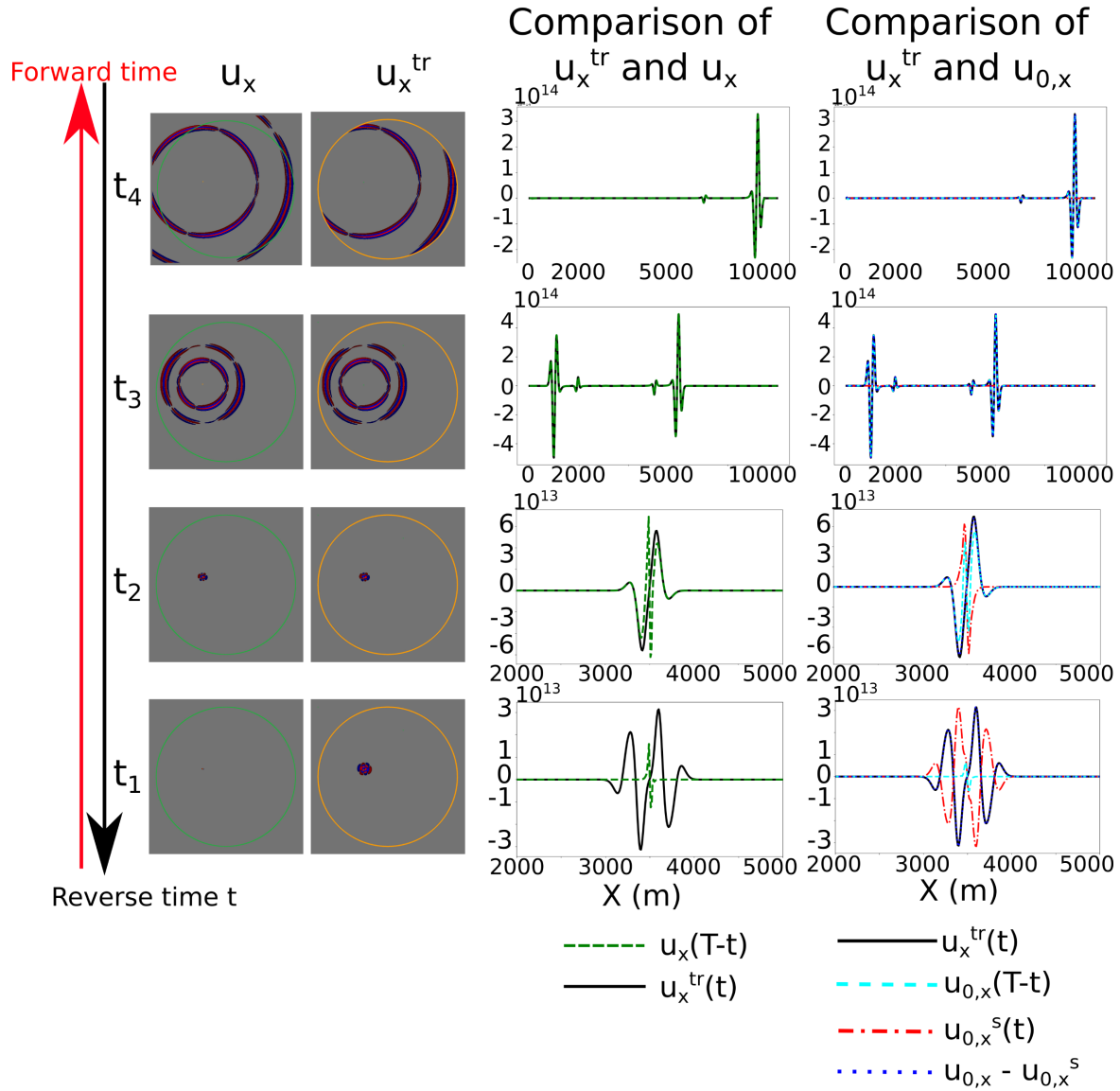
Figure 9. Comparison of the *x*-component of the backward displacement $\boldsymbol{u}^{tr}$ to the forward displacement $\boldsymbol{u}$ and to the point-source homogenization results $\boldsymbol{u}_0$ and $\boldsymbol{u}_0^s$. The two left-hand side columns show the forward and backward wavefields at four different time steps. The orange dots represent the sources and the green dots represent the receivers. The central column shows the forward and backward displacements along a line of receivers at forward source depth. The right-hand side column shows the two zeroth-order displacements $\boldsymbol{u}_0$ and $\boldsymbol{u}_0^s$, and compares the backward displacement to the difference $\boldsymbol{u}_0(\boldsymbol{x}, T - t) - \boldsymbol{u}_0^s(\boldsymbol{x}, t)$, which is the main result of the paper (eq. 33).

displacement does not match the forward displacement (central column) even if the two wavefields may look similar at a glance (left-hand columns). The forward displacement indeed shows a space discontinuity whereas the backward displacement remains smooth. The bottom row of the figure (t_1) also shows this discrepancy, and it illustrates what happens when the sink term is not implemented: the backward wavefield diverges from the source position whereas the forward wavefield reduces to a point before vanishing.

The curves in the right-hand side column of Fig. 9 show a comparison between the backward displacement $\boldsymbol{u}^{tr}$ and the zeroth-order displacement $\boldsymbol{u}_0$ and $\boldsymbol{u}_0^s$ computed from the homogenized point source. We observe that $\boldsymbol{u}_0(\boldsymbol{x}, T - t) - \boldsymbol{u}_0^s(\boldsymbol{x}, t)$ matches $\boldsymbol{u}^{tr}(\boldsymbol{x}, t)$ everywhere in space and time, which confirms eq. (33). The same conclusion can be drawn using the *z*-component.

4.2 An extended source in a homogeneous medium

Extended sources can represent finite fault ruptures. They can be discretized in space using elementary surfaces dS_i at position $\boldsymbol{x}_i$ (e.g. Yue & Lay 2020). In this case, the driving force can be written as

$$\boldsymbol{f}(\boldsymbol{x}, t) = \sum_i \boldsymbol{f}_i(\boldsymbol{x}, t), \tag{35}$$

$$f_i(x, t) = M_i \nabla \delta(x - x_i) g_i(t) dS_i, \tag{36}$$

where M_i is the moment tensor of the ith point source positioned at x_i (Aki & Richards 2002).

To derive our main result (33) in the case of an extended source discretized as multiple point sources, we rewrite eq. (9):

$$u^{tr}(x, t) = \sum_i u_i(x, T - t) - \sum_i u_i^s(x, t), \tag{37}$$

where u_i and u_i^s are the response to f_i and $f_i^s = f_i(x, T - t)$, respectively. Using the decomposition (19) for each of these displacements, eq. (37) becomes

$$u^{tr}(x, t) = \sum_i \left(u_{0,i}(x, T - t) + \theta_i(y) g_i(T - t) \right)$$
$$- \sum_i \left(u_{0,i}^s(x, t) + \theta_i^s(y) g_i(T - t) \right) + \mathcal{O}(\epsilon_0). \tag{38}$$

As in the single point-source case, the correctors θ_i and θ_i^s are equal for each point source independently. That leads to

$$u^{tr}(x, t) = \sum_i (u_{0,i}(x, T - t)) - \sum_i \left(u_{0,i}^s(x, t) \right) + \mathcal{O}'(\epsilon_0). \tag{39}$$

This last equation is equivalent to (33) in the case of multiple point sources.

To illustrate eq. (39), we perform a numerical experiment in the 10 km × 10 km homogeneous medium that we used in the previous sections. In this medium, we insert a horizontal finite fault discretized using four point sources. We choose the four corresponding moment tensors to be equal to each other, that is, $M_i = M \, \forall i$, where M is chosen arbitrarily:

$$M = \begin{bmatrix} 0.56 & 1 \\ 1 & 2.56 \end{bmatrix}. \tag{40}$$

We take the four source time functions g_i having the same Ricker shape, but we shift them according to the centroid time τ_i so that the rupture propagates toward the increasing point numbers: $\tau_1 < \tau_2 < \tau_3 < \tau_4$. Moreover, we want the fault segment displacements to overlap in time, so we choose $\Delta \tau = \tau_{i+1} - \tau_i = T_w/2$, with T_w the time support of the Ricker wavelet. Assuming a rupture speed equal to V_s, the length of the segments is calculated using $dS = V_s \Delta \tau$.

Fig. 10 shows that the time reversal focal spot obtained in the case of an extended source is more complex than the one obtained in the single point-source case. Despite this complexity, our theory holds: in the right-hand side column of the figure, eq. (39) is confirmed at three different times in the focalization time interval. The only difference from the single point-source case is that the computations of $u_0(x, t)$ and $u_0^s(x, t)$ have to be carried out separately: u_0 is computed based on the forward source order (i.e. $(x_1, \tau_1), (x_2, \tau_2),..., (x_n, \tau_n)$) whereas u_0^s is computed in the reverse order of the source position (i.e. $(x_n, \tau_1), (x_{n-1}, \tau_2),..., (x_1, \tau_n)$).

4.3 *P* and *S* waves in a heterogeneous medium

To emphasize the validity of our results in heterogeneous cases, we apply our theory to a realistic geological case: the Groningen gas field, which is known for its induced seismicity (van der Voort & Vanclay 2015; Hettema *et al.* 2017). The Groningen field is the largest gas reservoir in Europe. It is located in Northern Netherlands. The stratigraphy of the field and its overburden is given in Appendix B.

The velocity model we use (Fig. 11) is slightly modified from Romijn (2017). To avoid high computational costs due to small-scale features, we smooth this model of Groningen using the non-periodic homogenization of elastic properties (e.g. Capdeville *et al.* 2010, 2015; Cupillard & Capdeville 2018). Such a process prevents from small elements in wave simulations while maintaining an accurate solution. In Fig. 12, we see that geological patterns similar to the original model are clearly visible, but discontinuities have been smeared out.

To generate waves in this heterogeneous medium, we use the moment tensor introduced in Section 4.1 and place the source in the Zechstein salt layer (Appendix B). The source time function $g(t)$ is a Ricker wavelet with a maximum frequency of 15 Hz, which is a realistic frequency in Groningen (Spetzler & Dost 2017; Willacy *et al.* 2019). The complexity of the medium leads to a complex wavefield. Despite this complexity, we are able to describe the focal spot as the combination of two homogenized point sources. Fig. 13 shows that having heterogeneity in the medium does not alter the result presented in Section 3.2. The right-hand side column shows that the time reversal displacement u^{tr} at the focalization is a combination of two homogenized point-source displacements u_0 and u_0^s. This result is still valid if there are heterogeneities in the vicinity of the source location. In that case, it is necessary to compute an effective moment tensor taking those heterogeneities into account (Capdeville *et al.* 2010) and then apply the point-source homogenization theory to this moment tensor (Capdeville 2021).
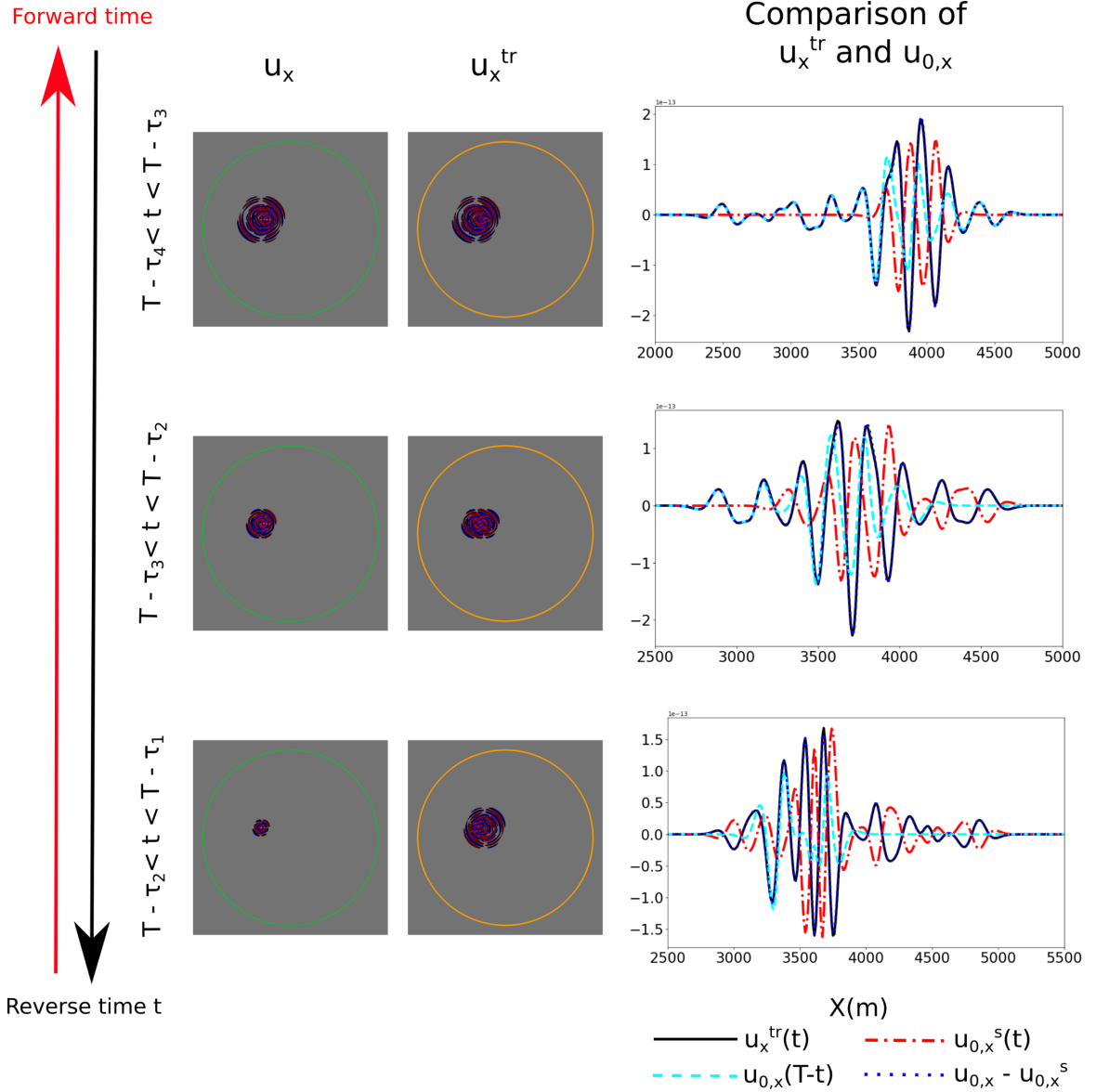
Figure 10. Left: the forward and backward wavefields in the case of an extended source made of four point sources. Three times in the focalization time interval are presented. Right: comparison between the backward displacement $\boldsymbol{u}^{tr}$ and the difference between the two zeroth-order displacements $\boldsymbol{u}_0$ and $\boldsymbol{u}_0^s$ obtained from the homogenization the four point sources. The black line is the backward u_x^{tr}, the red dashed one is the homogenized sink displacement $u_{0,x}^s$, the cyan dashed one is the homogenized forward displacement $u_{0,x}$ and the blue dashed one is the difference $u_{0,x} - u_{0,x}^s$.

5 DISCUSSION

As described by many works in the past, the time reversal wavefield is shown to be smooth at the source location whereas the wavefield generated by an earthquake presents a spatial discontinuity. Relying on the representation theorem and the point-source homogenization theory, we demonstrated a direct relation between the time reversal wavefield and the displacement generated by a homogenized point source (eq. 33). By homogenized point source, we mean the smooth effective source derived from the homogenization theory developed by Capdeville (2021). The relation is satisfied at all propagation times, including the focalization, which yields a new interpretation of the focal spot: this latter can be seen as the sum of two zeroth-order displacements generated by the smooth effective source.

Whereas considerable efforts have been made for spiking the focal spot (e.g. Kiser *et al.* 2011; Fukahata *et al.* 2014; Douma & Snieder 2014; Anderson *et al.* 2015; Bazargani & Snieder 2016; Nakata & Beroza 2016), our work leaves it intact and proposes to upscale the source model in order to derive smooth displacements that fit the focal spot. Such a process requires solving the static eq. (20), but then one no longer needs any small elements at the source location when simulating wave propagation numerically because the effective source is free of small scales. We did not illustrate this computational gain in this paper; we rather used the same fine mesh for all the simulations to avoid possible numerical bias and make our comparisons as accurate as possible.
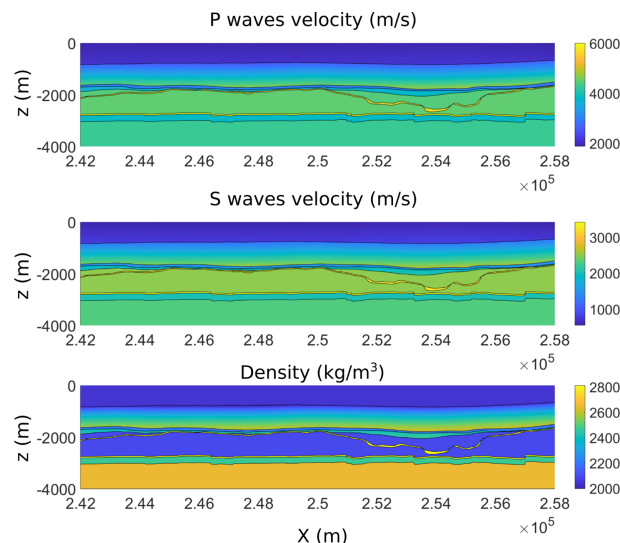
Figure 11. Elastic properties in a cross-section of the 3-D model of the Groningen gas field: *P*-wave velocity (top row) and *S*-wave velocity (middle row) and density (bottom row).
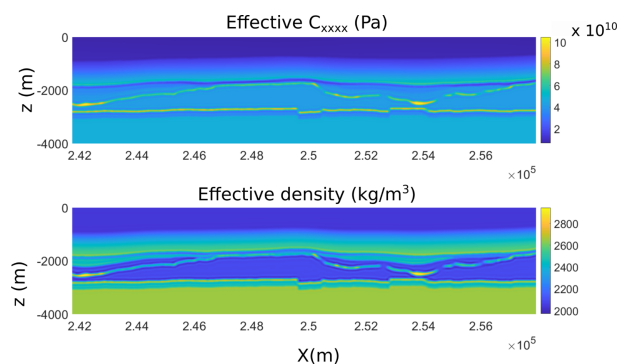

Figure 12. Cross-section of the 3-D homogenized model. The top line represents the first component of the homogenized elastic tensor and the bottom line is the homogenized density.

Once the upscaling process is known, downscaling the focal spot can be considered to estimate source model parameters. Adjoint tomography has been proved to successfully yield the moment tensor (Liu *et al.* 2004). As for the location, the inverse problem is highly nonlinear (Kim *et al.* 2011), which makes adjoint tomography computationally expensive. Moreover, this technique is deterministic, requiring an initial model and leading to a single solution that can correspond to a local minimum of the misfit function. Our result opens the path to a Bayesian inversion that could overcome these limitations. In such an inversion, the focal spot would be the data and the point-source homogenization would be the first step of the forward modelling operation. The second step would be the computation of a few time steps of the two zeroth-order wavefields, which consists of just one simulation in the case of a single point source and of two simulations in the case of multiple point sources. The main advantage of using a homogenized point source as compared to a classic point source is that the mesh can be coarse, so the simulation cost is low. The downscaling procedure we outline here is inspired by what Hedjazian *et al.* (2021) developed to estimate small-scale elastic properties.

It is worth noting that adjoint tomography also turns receivers into sources to backpropagate signals (e.g. Tromp *et al.* 2005). Interestingly, Kim *et al.* (2011) use a time reversal simulation as an adjoint wavefield to show how this latter captures the characteristics of the source. From a more practical point of view, time reversal can be used to avoid the storage of the whole forward simulation. Recording the forward wavefield along a close surface indeed allows to reconstruct it during the adjoint simulation so that the two wavefields can be correlated on the fly to efficiently compute the gradient of the misfit function. By doing so, the inverse problem can be solved without storing a large amount of data at each iteration.

Our theoretical result (33) was illustrated using numerical experiments in a simple 2-D homogeneous medium and in a more realistic 2-D heterogeneous medium. The result is valid in 3-D too. Nevertheless, for applications to real cases, the time reversal assumptions presented in the introduction become unreachable for good: (i) the closed mirror is impossible to set, (ii) the velocity model is never completely known, there are still uncertainties and (iii) there is attenuation. In the following of this discussion, we are going to investigate points (i) and (ii), the attenuation being neglected in most of earthquake location methods and some mathematical and numerical solutions being available to take it into account (e.g. Zhu 2014; Bai *et al.* 2019).
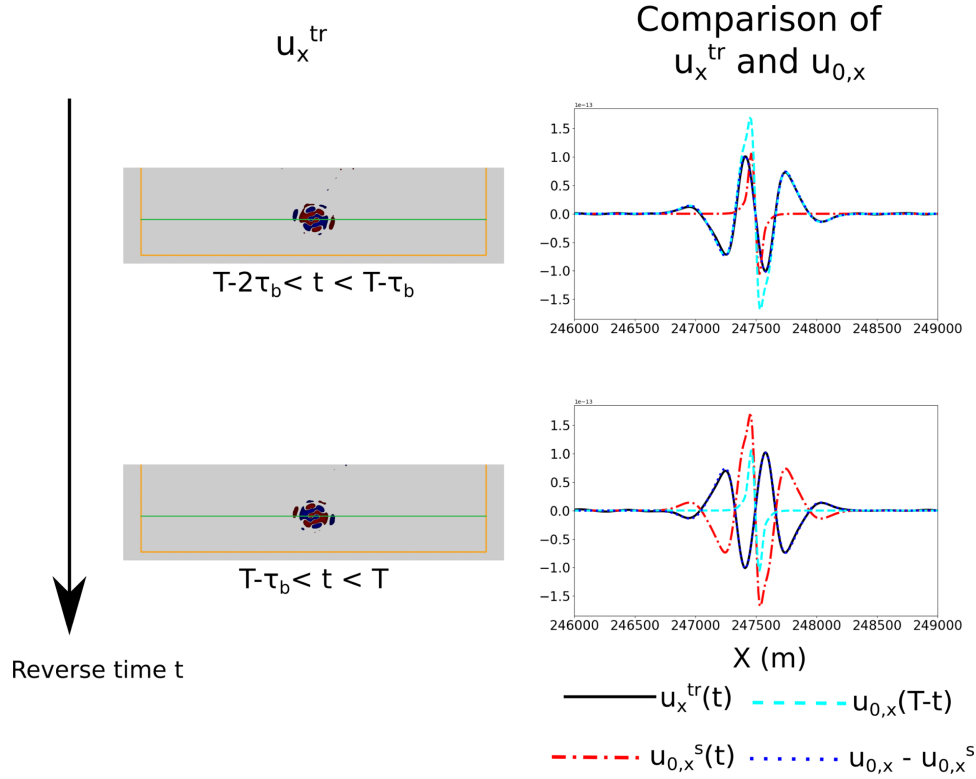
u_x^{tr}

Comparison of u_x^{tr} and $u_{0,x}$

$T-2\tau_b < t < T-\tau_b$

$T-\tau_b < t < T$

Reverse time t

X (m)

——— $u_x^{tr}(t)$ – – – – $u_{0,x}(T-t)$

—·—·— $u_{0,x}^s(t)$ ········· $u_{0,x} - u_{0,x}^s$

Figure 13. Comparison of the *x*-component of the backward displacement $\boldsymbol{u}^{tr}$ and the point-source homogenization results $\boldsymbol{u}_0$ and $\boldsymbol{u}_0^s$. The left-hand side column shows the backward wavefield at two different times of the focalization. The orange dots represent the sources and the green line represents receivers for the comparison on the right-hand side column. This column shows the two zeroth-order displacements $\boldsymbol{u}_0$ and $\boldsymbol{u}_0^s$, and compares the backward displacement to the difference $\boldsymbol{u}_0(\boldsymbol{x}, T-t) - \boldsymbol{u}_0^s(\boldsymbol{x}, t)$.
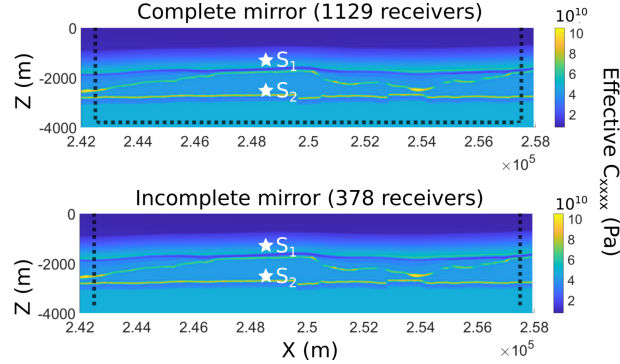

Figure 14. Geometry of the two time reversal mirrors. On the top row, the complete mirror is composed of 1129 receivers (spacing = 20 m). On the bottom row, the incomplete mirror is composed of two vertical wells with 378 receivers (spacing = 20 m). The white stars represent the two source positions which are tested.

5.1 Impact of an incomplete time reversal mirror

Some sensitivity studies have already been performed to investigate the impact of a partial mirror on time reversal. Gajewski & Tessmer (2005) showed that the spacing of receivers at the surface of the earth impacts the quality of the wavefield reconstruction but has a week influence on the focal spot location in space and time. Bazargani & Snieder (2016) showed that the localization of the source depends on the source position with respect to the mirror and to reflecting interfaces. However, to determine what happens to our result when a partial mirror is involved, we need to know how it modifies the wavefield of the focal spot. To outline an answer to that question, we perform primarily tests in the model of the Groningen gas field (Fig. 12).

We compare results of backward simulations from a complete mirror on one hand and from an incomplete mirror on the other hand. The latter is somewhat realistic case: it consist in two vertical wells. Two different source positions are considered (Fig. 14). For sake of simplicity, the two sources are explosions. We do not put any receiver at the surface because a free surface act as a natural mirror by reflecting all the waves inside the medium.
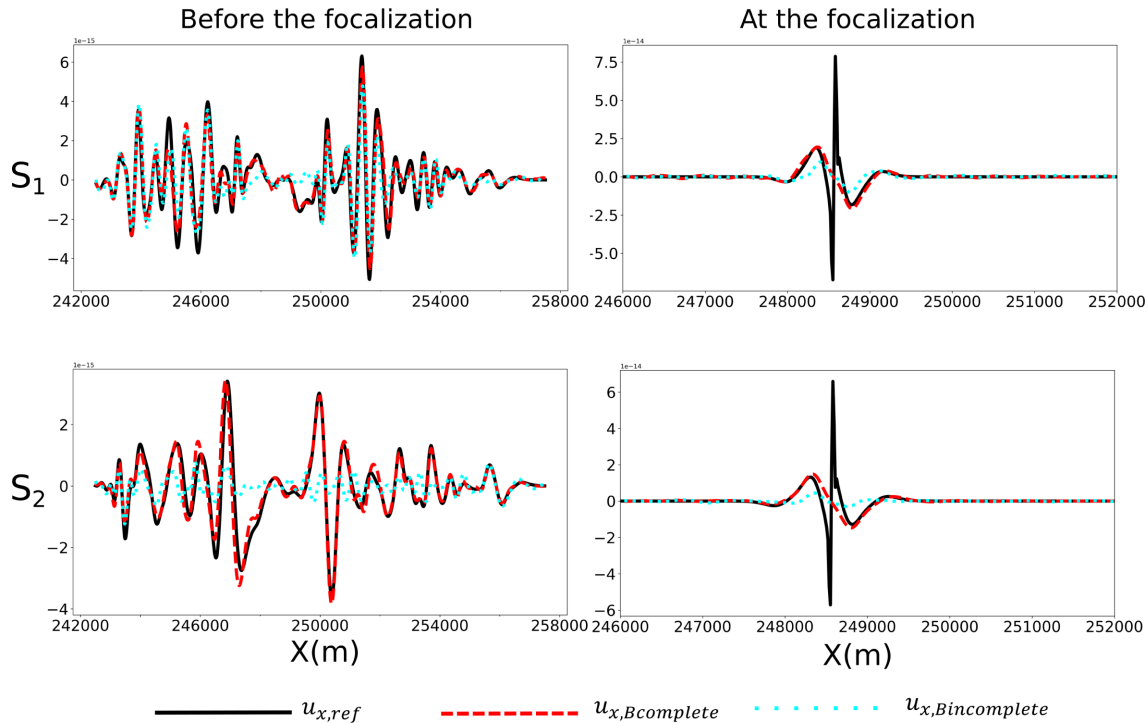
Figure 15. Plot of the *x*-component of the displacement along a line which is set at the source depth and for two different time steps. The left-hand side column is before the focalization and the right-hand side column is at the focalization. The black line represents the forward displacement u_{ref}, the red dashed line the backward displacement obtained with the complete mirror $u_{B complete}$ and the cyan dotted line the backward displacement obtained with the incomplete mirror.

Fig. 15 shows the *x*-component of the displacement along a line of receivers at two different times and for each source. Looking at the results from the complete mirror, we see the backward wavefield away from the focalization fits the forward wavefield (Fig. 15, left-hand side column). The slight differences in amplitude are due to the fact that the forward simulation is stopped when there is still a bit of energy in the medium so that some energy is missing in the backward simulation. At the focalization (Fig. 15, right-hand side column), we retrieve what we observe in the previous part: the backward wavefield is a smooth version of the forward wavefield. If we now look at the backward wavefield from the incomplete mirror, we see that the results are different from one source to the other. Before the focalization, the results are better for the source S_1: most of the wiggles are retrieved, differences in amplitude being due to the different amount of energy recorded in the complete and in the incomplete cases. For the source S_2, very few wiggles are reconstructed. At the focalization, nonetheless, the difference between S_1 and S_2 is less obvious: although weaker than in the complete mirror case, a clear focal spot emerges. The latter looks like having a higher wave number content, but it is still centred at the source position. In the current state of knowledge, such a focal spot is not a sum of two wavefields generated from the homogenization of the true source, but its shape suggests that it holds information similar to those contained in the complete mirror focal spot. This quantitative observations is promising for further research to be successful in relating incomplete mirror focal spot to point-source homogenization.

5.2 Impact of the velocity model uncertainties

The knowledge of the subsurface geometry and properties is key to locate an earthquake precisely. However, in real cases, there are uncertainties on the subsurface structures in which the wave propagate and on the velocity in which we perform the time reversal. For example in the Groningen gas field, there are a lot of uncertainties in the Zechstein formation (Fig. 16).

For instance, in the acoustic case, these uncertainties can have a impact on the source location in space and time. Gajewski & Tessmer (2005) show in acoustic case that the shift is about one period in time and one dominant wavelength in space when the forward simulation is performed in a random medium with the same range of wave velocities as in the true medium. Using a smooth version of the true velocity model, these authors showed that there is no impact on the source location and a small impact on the centroid time (i.e. below the dominant period). Bazargani & Snieder (2016) performed the same type of experiments and confirmed these results. However in the case of the Groningen gas field, the uncertainties do not keep the velocity range constant so we can expect that the impact on the focal spot position in time and space to be more significant than the one obtained by Gajewski & Tessmer (2005) and Bazargani & Snieder (2016). Furthermore, these works do not study the impact of the model uncertainties on the wavefield in the focal spot. Similarly to the results obtained when investigating the impact of a partial mirror (Section 5.1), our derivation would degrade when the velocity model significantly deviates from the true earth. In particular, there would be no guarantee that the focal spot keeps the shape of the sum of two wavefields originating from a homogenized point source.
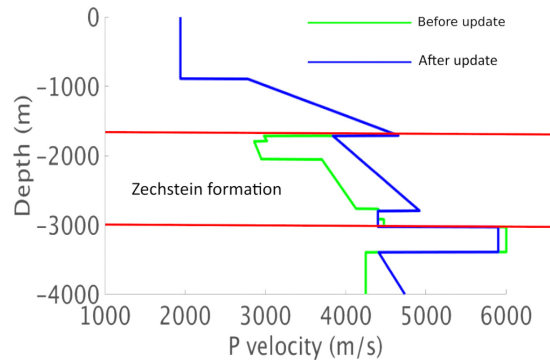
Figure 16. 1-D profile of the *P*-wave velocity before (green) and after (blue) the model update proposed by Romijn (2017). The largest uncertainties lie in the Zechstein formation (see Appendix B).

6 CONCLUSION

We demonstrated that there is a direct relation between point-source homogenization and time reversal. This relation provides a new interpretation of the time reversal focal spot, which can be seen as a sum of two zeroth-order wavefields generated by a smooth effective source. This results comes as a complement to previous theoretical studies on the subject (e.g. Kawakatsu & Montagner 2008; Fukahata *et al.* 2014; Kiser *et al.* 2011; Douma & Snieder 2014; Anderson *et al.* 2015; Nakahara & Haney 2015). Its opens the path to the downscaling of focal spots for determining source mechanisms. To achieve this long-term goal, introducing an incomplete mirror and uncertainties on the propagation medium in our theory will be necessary.

ACKNOWLEDGMENTS

DATA AVAILABILITY

The point-source homogenization software underlying this paper is available on demand. SpecFEM2D is accessible at https://github.com/geodynamics/specfem2d and the branch containing the time reversal method is available on demand.

REFERENCES

Aki, K. & Richards, P.G., 2002. *Quantitative Seismology,* University Science Books, 2nd edn.

Anderson, B.E., Douma, J., Ulrich, T. & Snieder, R., 2015. Improving spatio-temporal focusing and source reconstruction through deconvolution, *Wave Motion,* **52,** 151–159.

Bai, T., Zhu, T. & Tsvankin, I., 2019. Attenuation compensation for time-reversal imaging in VTI media, *Geophysics,* **84**(4), C205–C216.

Bazargani, F. & Snieder, R., 2016. Optimal source imaging in elastic media, *Geophys. J. Int.,* **204**(2), 1134–1147.

Borcea, L., Papanicolaou, G. & Tsogka, C., 2003. Theory and applications of time reversal and interferometric imaging, *Inverse Probl.,* **19**(6), S139–S164.

Cao, W., Hanafy, S.M., Schuster, G.T., Zhan, G. & Boonyasiriwat, C., 2012. High-resolution and super stacking of time-reversal mirrors in locating seismic sources, *Geophys. Prospect.,* **60**(1), 1–17.

Capdeville, Y., 2021. Homogenization of seismic point and extended sources, *Geophys. J. Int.,* **226**(2), 1390–1416.

Capdeville, Y., Guillot, L. & Marigo, J.-J., 2010. 2-D non-periodic homogenization to upscale elastic media for P - SV waves, *Geophys. J. Int.,* **182**(2), 903–922.

Capdeville, Y., Zhao, M. & Cupillard, P., 2015. Fast Fourier homogenization for elastic wave propagation in complex media, *Wave Motion,* **54,** 170–186.

Capdeville, Y., Cupillard, P. & Singh, S., 2020. An introduction to the two-scale homogenization method for seismology, in *Advances in Geophysics,* Vol. **61,** pp. 217–306, Elsevier.

Cassereau, D. & Fink, M., 1992. Time-reversal of ultrasonic fields—Part III: theory of the closed time-reversal cavity, *IEEE Trans. Ultrason. Ferroelectr. Freq. Control,* **39**(5), 579–592.

Chambers, K., Dando, B.D., Jones, G.A., Velasco, R. & Wilson, S.A., 2014. Moment tensor migration imaging, *Geophys. Prospect.,* **62**(4), 879–896.

Cros, E., Roux, P., Vandemeulebrouck, J. & Kedar, S., 2011. Locating hydrothermal acoustic sources at Old Faithful Geyser using Matched Field Processing, *Geophys. J. Int.,* **187**(1), 385–393.

Cupillard, P. & Capdeville, Y., 2018. Non-periodic homogenization of 3-D elastic media for the seismic wave equation, *Geophys. J. Int.,* **213**(2), 983–1001.

De Jager, J. & Visser, C., 2017. Geology of the Groningen field—an overview, *Geol. en Mijnbouw/Netherlands J. Geosci.,* **96**(5), s3–s15.

de Rosny, J. & Fink, M., 2002. Overcoming the diffraction limit in wave physics using a time-reversal mirror and a novel acoustic sink, *Phys. Rev. Lett.,* **89**(12), 124301.

Douma, J. & Snieder, R., 2014. Focusing of elastic waves for microseismic imaging, *Geophys. J. Int.,* **200**(1), 390–401.

Douma, J., Niederleithinger, E. & Snieder, R., 2015. Locating events using time reversal and deconvolution: experimental application and analysis, *J. Nondestruct. Eval.,* **34**(1), 1–9.

Draeger, C. & Fink, M., 1997. One-channel time reversal of elastic waves in a chaotic 2D-silicon cavity, *Phys. Rev. Lett.,* **79**, 407–410.

Finger, C. & Saenger, E.H., 2021. Determination of the time-dependent moment tensor using time reverse imaging, *Geophysics,* **86**(2), KS63–KS77.

Fink, M., 1992. Time reversal of ultrasonic fields—Part I: basic principles, *IEEE Trans. Ultrason. Ferroelectr. Freq. Control,* **39**(5), 555–566.

Fink, M., 2006. Time-reversal acoustics in complex environments, *Geophysics,* **71**(4), SI151–SI164.

Fink, M., 2015. Acoustic imaging with time reversal methods: From medicine to ndt, in *AIP Conference Proceedings,* Vol. **1650,** pp. 13–23, American Institute of Physics.

Fukahata, Y., Yagi, Y. & Rivera, L., 2014. Theoretical relationship between back-projection imaging and classical linear inverse solutions, *Geophys. J. Int.,* **196**(1), 552–559.

Gajewski, D. & Tessmer, E., 2005. Reverse modelling for seismic event characterization, *Geophys. J. Int.,* **163**(1), 276–284.

Garmany, J., 1979. On the inversion of travel times, *Geophys. Res. Lett.,* **6**(4), 277–279.

Gelius, L.-J. & Asgedom, E., 2011. Diffraction-limited imaging and beyond—the concept of super resolution‡, *Geophys. Prospect.,* **59**(3), 400–421.

Givoli, D. & Turkel, E., 2012. Time reversal with partial information for wave refocusing and scatterer identification, *Comput. Methods Appl. Mech. Eng.,* **213-216,** 223–242.

Grigoli, F., Cesca, S., Krieger, L., Kriegerowski, M., Gammaldi, S., Horalek, J., Priolo, E. & Dahm, T., 2016. Automated microseismic event location using Master-Event Waveform Stacking, *Sci. Rep.,* **6**(1), 25744.

Hampson, D. & Russell, B., 1984. First–break interpretation using generalized linear inversion, in *SEG Tech. Progr. Expand. Abstr. 1984,* pp. 532–534, Society of Exploration Geophysicists.

Hedjazian, N., Capdeville, Y. & Bodin, T., 2021. Multiscale seismic imaging with inverse homogenization, *Geophys. J. Int.,* **226**(1), 676–691.

Hettema, M.H., Jaarsma, B., Schroot, B.M. & Van Yperen, G.C., 2017. An empirical relationship for the seismic activity rate of the Groningen gas field, *Geol. en Mijnbouw/Netherlands J. Geosci.,* **96**(5), s149–s161.

Ishii, M., Shearer, P.M., Houston, H. & Vidale, J.E., 2007. Teleseismic p wave imaging of the 26 december 2004 sumatra-andaman and 28 march 2005 sumatra earthquake ruptures using the hi-net array, *J. geophys. Res.: Solid Earth,* **112**(B11), 307.

Kao, H. & Shan, S.-J., 2004. The Source-Scanning Algorithm: mapping the distribution of seismic sources in time and space, *Geophys. J. Int.,* **157**(2), 589–594.

Kawakatsu, H. & Montagner, J.-P., 2008. Time-reversal seismic-source imaging and moment-tensor inversion, *Geophys. J. Int.,* **175**(2), 686–688.

Kennett, B.L. & Sambridge, M.S., 1992. Earthquake location - genetic algorithms for teleseisms, *Phys. Earth planet. Inter.,* **75**(1–3), 103–110.

Kim, Y., Liu, Q. & Tromp, J., 2011. Adjoint centroid-moment tensor inversions, *Geophys. J. Int.,* **186**(1), 264–278.

Kiser, E., Ishii, M., Langmuir, C.H., Shearer, P.M. & Hirose, H., 2011. Insights into the mechanism of intermediate-depth earthquakes from source properties as imaged by back projection of multiple seismic phases, *J. geophys. Res.: Solid Earth,* **116**(B6), 306.

Komatitsch, D. & Tromp, J., 1999. Introduction to the spectral element method for three-dimensional seismic wave propagation, *Geophys. J. Int.,* **139**(3), 806–822.

Komatitsch, D. & Vilotte, J.-P., 1998. The spectral element method: an efficient tool to simulate the seismic response of 2D and 3D geological structures, *Bull. seism. Soc. Am.,* **88**(2), 368–392.

Kremers, S., Fichtner, A., Brietzke, G.B., Igel, H., Larmat, C., Huang, L. & Käser, M., 2011. Exploring the potentials and limitations of the time-reversal imaging of finite seismic sources, *Solid Earth,* **2**(1), 95–105.

Kruiver, P.P. *et al.*, 2017. An integrated shear-wave velocity model for the Groningen gas field, The Netherlands, *Bull. Earthq. Eng.,* **15**(9), 3555–3580.

Kuperman, W., Hodgkiss, W.S., Song, H.C., Akal, T., Ferla, C. & Jackson, D.R., 1998. Phase conjugation in the ocean: experimental demonstration of an acoustic time-reversal mirror, *J. acoust. Soc. Am.,* **103**(1), 25–40.

Larmat, C., Montagner, J.P., Fink, M., Capdeville, Y., Tourin, A. & Clévédé, E., 2006. Time-reversal imaging of seismic sources and application to the great Sumatra earthquake, *Geophys. Res. Lett.,* **33**(19), 0–3.

Larmat, C., Tromp, J., Liu, Q. & Montagner, J.P., 2008. Time reversal location of glacial earthquakes, *J. geophys. Res. Solid Earth,* **113**(9), 1–9.

Lerosey, G., de Rosny, J., Tourin, A. & Fink, M., 2007. Focusing beyond the diffraction limit with far-field time reversal, *Science (80-.).,* **315**(5815), 1120–1122.

Li, L. *et al.*, 2020. Recent advances and challenges of waveform–based seismic location methods at multiple scales, *Rev. Geophys.,* **58**(1), 1–47.

Li, Z. & van der Baan, M., 2016. Microseismic event localization by acoustic time reversal extrapolation, *Geophysics,* **81**(3), KS123–KS134.

Liu, Q., Polet, J., Komatitsch, D. & Tromp, J., 2004. Spectral-element moment tensor inversions for earthquakes in southern california, *Bull. seism. Soc. Am.,* **94**(5), 1748–1761.

Masson, Y. & Romanowicz, B., 2017. Fast computation of synthetic seismograms within a medium containing remote localized perturbations: a numerical solution to the scattering problem, *Geophys. J. Int.,* **208**(2), 674–692.

Masson, Y., Cupillard, P., Capdeville, Y. & Romanowicz, B., 2014. On the numerical implementation of time-reversal mirrors for tomographic imaging, *Geophys. J. Int.,* **196**(3), 1580–1599.

McMechan, G.A., 1982. Determination of source parameters by wavefield extrapolation, *Geophys. J. Int.,* **71**(3), 613–628.

Milne, J., 1886. *Earthquakes and Other Earth Movements,* Vol. **56,** K. Paul, Trench.

Nakahara, H. & Haney, M.M., 2015. Point spread functions for earthquake source imaging: an interpretation based on seismic interferometry, *Geophys. J. Int.,* **202**(1), 54–61.

Nakata, N. & Beroza, G.C., 2016. Reverse time migration for microseismic sources using the geometric mean as an imaging condition, *Geophysics,* **81**(2), KS51–KS60.

Rabinovich, D., Turkel, E. & Givoli, D., 2018. An augmented time reversal method for source and scatterer identification, *J. Comput. Phys.,* **375**(August), 99–119.

Rietbrock, A. & Scherbaum, F., 1994. Acoustic imaging of earthquake sources from the Chalfant Valley, 1986, aftershock series, *Geophys. J. Int.,* **119**(1), 260–268.

Romijn, R., 2017. *Groningen Velocity Model 2017 - Groningen full elastic velocity model,* Tech. rep., NAM.

Sambridge, M. & Mosegaard, K., 2002. Monte Carlo methods in geophysical inverse problems, *Rev. Geophys.,* **40**(3), 3–1-3-29.

Schuster, G.T., Yu, J., Sheng, J. & Rickett, J., 2004. Interferometric/daylight seismic imaging, *Geophys. J. Int.,* **157**(2), 838–852.

Schuster, G.T., Hanafy, S. & Huang, Y., 2012. Theory and feasibility tests for a seismic scanning tunnelling macroscope, *Geophys. J. Int.,* **190**(3), 1593–1606.

Shi, P., Angus, D., Rost, S., Nowacki, A. & Yuan, S., 2019. Automated seismic waveform location using multichannel coherency migration (MCM)–I: theory, *Geophys. J. Int.,* **216**(3), 1842–1866.

Shustak, M. & Landa, E., 2017. Time reversal based detection of subsurface scatterers, in *SEG Tech. Progr. Expand. Abstr. 2017,* pp. 969–973, Society of Exploration Geophysicists.

Spetzler, J. & Dost, B., 2017. Hypocentre estimation of induced earthquakes in Groningen, *Geophys. J. Int.,* **209**(1), 453–465.

Steiner, B., Saenger, E.H. & Schmalholz, S.M., 2008. Time reverse modeling of low-frequency microtremors: application to hydrocarbon reservoir localization, *Geophys. Res. Lett.,* **35**(3), 1–7.

Tolsma, S., 2014. *Seismic characterization of the Zechstein carbonates in the Dutch northern offshore,* PhD thesis, Utrecht University.

Tromp, J., Tape, C. & Liu, Q., 2005. Seismic tomography, adjoint methods, time reversal and banana-doughnut kernels, *Geophys. J. Int.,* **160**(1), 195–216.

van der Voort, N. & Vanclay, F., 2015. Social impacts of earthquakes caused by gas extraction in the Province of Groningen, The Netherlands, *Environ. Impact Assess. Rev.,* **50**, 1–15.

van Manen, D.-J., Curtis, A. & Robertsson, J.O., 2006. Interferometric modeling of wave propagation in inhomogeneous elastic media using time reversal and reciprocity, *Geophysics,* **71**(4), SI47–SI60.

Willacy, C., van Dedem, E., Minisini, S., Li, J., Blokland, J.-W., Das, I. & Droujinine, A., 2019. Full-waveform event location and moment tensor inversion for induced seismicity, *Geophysics,* **84**(2), KS39–KS57.

Yang, J. & Zhu, H., 2019. Locating and monitoring microseismicity, hydraulic fracture and earthquake rupture using elastic time-reversal imaging, *Geophys. J. Int.,* **216**(1), 726–744.

Yue, H. & Lay, T., 2020. Resolving complicated faulting process using multi-point-source representation: iterative inversion algorithm improvement and application to recent complex earthquakes, *J. geophys. Res. Solid Earth,* **125**(2), 1–24.

Zhao, M., Capdeville, Y. & Zhang, H., 2016. Direct numerical modeling of time-reversal acoustic subwavelength focusing, *Wave Motion,* **67**, 102–115.

Zhu, T., 2014. Time-reverse modelling of acoustic wave propagation in attenuating media, *Geophys. J. Int.,* **197**(1), 483–494.

APPENDIX A: TWO-SCALE DECOMPOSITION OF THE DIRAC FUNCTION

The goal of this appendix is to demonstrate eq. (15). We first separate the small and large wavenumbers in a Dirac function using the low-pass filter F^{ϵ_0}:

$$\delta(\boldsymbol{x}) = F^{\epsilon_0}(\delta(\boldsymbol{x})) + (I - F^{\epsilon_0})(\delta(\boldsymbol{x})). \tag{A1}$$

Then we introduce F, the same filter than F^{ϵ_0} for the variable $\boldsymbol{y} = \frac{\boldsymbol{x}}{\epsilon_0}$. In other words, for any functions $h(\boldsymbol{x})$ and $\bar{h}(\boldsymbol{y}) = h(\epsilon_0 \boldsymbol{y})$, we have

$$F^{\epsilon_0}(h(\boldsymbol{x})) = F(\bar{h}(\boldsymbol{x}/\epsilon_0)). \tag{A2}$$

Using this last equality in eq. (A1), it comes

$$\delta(\boldsymbol{x}) = F^{\epsilon_0}(\delta(\boldsymbol{x})) + (I - F)(\delta(\epsilon_0 \boldsymbol{y})). \tag{A3}$$

Finally, we note the following property of the Dirac function:

$$\delta(\epsilon_0 \boldsymbol{y}) = \frac{1}{\epsilon_0} \delta(\boldsymbol{y}). \tag{A4}$$

Introducing eq. (A4) in eq. (A3), we obtain eq. (15).

APPENDIX B: GEOLOGICAL MODEL OF THE GRONINGEN GAS FIELD

The model of the gas field proposed by De Jager & Visser (2017) and Kruiver *et al.* (2017) is composed of eight geological formations (Fig. A1). The gas lies in Rotliegend sandstone and the top of the reservoir varies from 2600 to 3200 m. The cap rock is the Zechstein formation which can be decomposed in multiple layers of evaporites and carbonate deposits (Tolsma 2014).
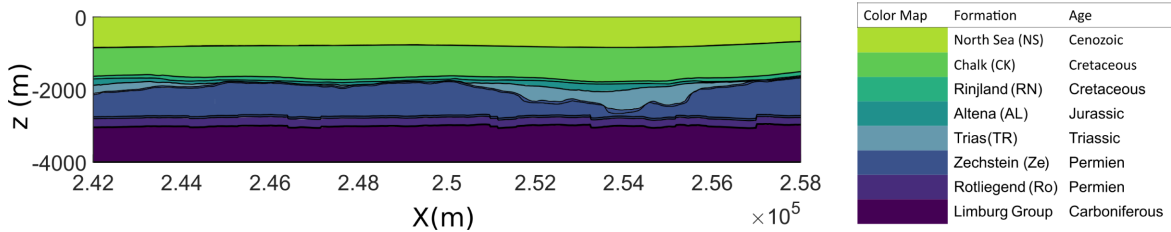

Figure A1. Cross-section of the 3-D geological model of the Groningen gas field (De Jager & Visser 2017; Kruiver *et al.* 2017).